DOI:
10.1021/acs.jpcc.7b03965

Document Version
Peer reviewed version

Near-field Raman Enhancement of Single Molecules and Point Scatterers

Sandro Mignuzzi,[1,*] Fumin Huang,[2] Debdulal Roy[1], David Richards,[1,*]

[1] *Department of Physics, King's College London, Strand, London WC2R 2LS, United Kingdom*

[2] *Centre for Nanostructured Media, School of Mathematics and Physics, Queen's University Belfast, University Road, Belfast, BT7 1NN, United Kingdom*

[a] *sandro.mignuzzi@kcl.ac.uk*

[b] *david.r.richards@kcl.ac.uk*

ABSTRACT

Tip-enhanced Raman spectroscopy (TERS) is an emerging tool to characterize low-dimensional materials requiring high spatial resolution beyond light diffraction limit. The most extreme example of a spatially localized scatterer is that of a zero-dimensional (0-D) system, e.g. a single molecule, a nanoparticle, or an individual defect within a crystal. Here, using an analytical model for near-field Raman scattering from point-like structures in the presence of a plasmonic metal probe, we investigate the TERS patterns of representative single molecules with arbitrary orientation, for a range of Raman tensor symmetries. The results can be used to determine the orientation of single molecules as well as to differentiate molecules with diverse Raman tensors, or, conversely, Raman modes with different Raman tensors from the same molecule. To demonstrate that the model is of general applicability to any spatially localized Raman modes, we further apply it to TERS imaging of individual point defects in graphene, unveiling the dependence of field enhancement and spatial resolution on the Raman mode symmetry, incident field polarization and angle of the near-field probe.

I. INTRODUCTION

Recent developments in nanotechnology have been supported by Raman spectroscopy as a non-destructive and versatile characterization technique for the study of nanomaterials. However, Raman spectroscopy, in its widely used confocal configuration, is a diffraction-limited technique which is often not suitable for the study of spatially localized scatterers, often encountered within a broad range of nanomaterials. Spatial confinement down to the nanometer-scale gives rise to a variety of low-dimensional materials and structures, which can be classified as zero-dimensional (0-D), one-dimensional (1-D) and two-dimensional (2-D) systems. Moreover, any nanometer disruption or alteration of translational symmetry in a crystalline bulk (i.e. 3-D) material can be regarded as a low-dimensional structure itself, which may locally alter its vibrational properties or allow normally forbidden vibrational modes to participate in Raman scattering.

Recently, near-field optical techniques have received a growing interest as a means to overcome the limitations of confocal Raman scattering[1]. In near-field Raman spectroscopy, typically, a metal probe acts as an optical antenna to convert the localized energy carried by the Raman near-field signal to an irradiating far-field signal (and *vice versa*), thus improving the spatial resolution down to the subwavelength regime[1,2]. Due to resonant excitation of surface plasmon polaritons on the metal probe, both the exciting and the scattered Raman fields are locally enhanced, improving the measurement sensitivity, in a similar fashion to surface enhanced Raman spectroscopy[1,2]. Such tip-enhanced Raman spectroscopy (TERS) has been used to characterize the Raman signatures of 0-D systems such as fullerenes under pressure[3], single molecules[4–8], and have been widely applied to map localized Raman scatterers embedded in both 1-D and 2-D systems[9–15]. In particular, in carbon nanotubes, near-field studies have been reported on: structural defects[16], semiconductor-to-metal transitions[10], changes in electronic and vibrational properties near dopants[17] and strain[12]. On the other hand, near-field optical spectroscopy is emerging as a valuable tool for the investigation of nanotubes' 2-D counterpart, graphene, with a particular focus on disorder-induced Raman scattering at edges[18]. TERS has also recently enabled direct spatial location and enumeration of single point defects within a graphene layer [9].

The ability to enhance and resolve extremely weak Raman scattering signatures is the ultimate goal of near-field Raman spectroscopy, and this is especially true for 0-D features, i.e. point scatterers. As a direct consequence, both the enhancement factor and the spatial resolution are key parameters to optimize; hence these are systematically determined in the vast majority of studies[2]. However, a near-field measurement can be influenced by several different factors which make the results highly dependent on the measurement conditions, i.e. probe-sample distance, experimental geometry, plasmonic properties of the probe, polarizability and dimensionality of the sample. Due to the variety and complexity of parameters to be taken into account it is often common to neglect these factors and to report the overall signal enhancement value only, thus hindering the comparability between different measurements.

Numerical methods are often used to gain quantitative insight into the value of enhancement; however, such studies usually provide a strong emphasis on the modelling of the probe optical

properties, neglecting the probe-sample interplay[19]. Simpler analytical approaches are instead preferred both for practical utility and because they allow a qualitative insight to the near-field mechanisms. Analytical models have been published for bulk crystals[20] and for 2-D[21] and 1-D [22] systems, as reported by Novotny and co-workers, also highlighting the importance of coherence[23,24]. In this article, we study near-field Raman scattering by 0-D systems, using an analytical model which can be applied to nanomaterials, molecules, and localized Raman scattering processes occurring in crystals. The model is applied here to localized defect-induced Raman scattering occurring at point defects in graphene and to representative biological molecules. We uncover the interplay between probe angle, probe-sample distance and Raman mode symmetry, and we show how these affect the enhancement and spatial resolution.

II. THEORY

In this section we outline a model for near-field Raman scattering [25–28] , applied to 0-D sources, with the purpose of gaining insight into the underlying principles behind the resulting enhancement and spatial resolution.

The geometry used for the model is schematically depicted in Fig.1. When the probe-sample system is excited by an incident electric field, both the probe and the sample undergo multiple scattering events. The case of interest, which gives the most significant Raman signal at the detector, is the one where the following steps occur: (i) the incident field is enhanced by the probe, (ii) the enhanced field excites the sample, (iii) the excited Raman signal is enhanced by the probe and then collected.

Using a dipole-dipole interaction model[17] (see Supporting Information for further details), the collected field intensity $\mathbf{I}$ assumes the form

$$\mathbf{I} \propto \frac{\omega^4 {\omega_S}^4}{{\varepsilon_0}^4 c^8} \left| \bar{\bar{\boldsymbol{\alpha}}}_{\mathrm{p}}(\omega_S) \cdot \bar{\bar{\mathbf{G}}}(\mathbf{r}', \mathbf{r_z}; \omega_S) \cdot \bar{\bar{\boldsymbol{\alpha}}}_{\mathrm{R}}(\omega_S, \omega) \cdot \bar{\bar{\mathbf{G}}}(\mathbf{r_z}, \mathbf{r}'; \omega) \cdot \bar{\bar{\boldsymbol{\alpha}}}_{\mathrm{p}}(\omega) \cdot \mathbf{E_i}(\mathbf{r}, \omega) \right|^2, \tag{1}$$

where $\mathbf{E_i}$ is the incident electric field, $\bar{\bar{\boldsymbol{\alpha}}}_{\mathrm{p}}$, $\bar{\bar{\boldsymbol{\alpha}}}_{\mathrm{R}}$ are the polarizabilities of the probe and of the Raman scatterer, respectively, $\bar{\bar{\mathbf{G}}}$ the free space Green's function. The terms ω, ω_S, ε_0, c, are the incident electric field frequency, the Raman frequency, the permittivity and the speed of light in vacuum, respectively. Fixing the position of the Raman scatterer at $\mathbf{r}' = (\mathbf{0}, \mathbf{0}, \mathbf{0})$, i.e. underneath the probe apex, Eq. 1 can be simplified to

$$\mathbf{I} \propto \frac{\rho^{12}}{\mathbf{16}\,(\Delta+\rho)^{\mathbf{12}}} {E_i}^2 \left| \tilde{f}(\omega)\, \tilde{f}(\omega_S) \right|^2 [\cos\gamma \cos\theta + \cos(\beta - \phi) \sin\gamma \sin\theta\,]^2 \{4\alpha_{33} \cos^2\theta - \sin 2\theta\, [(\alpha_{13} + \alpha_{31}) \cos\phi + (\alpha_{23} + \alpha_{32}) \sin\phi] + \sin^2\theta\, [\alpha_{11} \cos^2\phi + (\alpha_{12} + \alpha_{21}) \cos\phi \sin\phi + \alpha_{22} \sin^2\phi]\}^2 . \tag{2}$$

The angles $\gamma, \theta, \beta, \phi$, are depicted in Figure 1. Δ is the tip-surface separation, ρ is the radius of curvature of the tip and α_{ij} are the components of the Raman tensor $\bar{\bar{\boldsymbol{\alpha}}}_{\mathrm{R}}$. From Eq. 2, we note that the Raman intensity is inversely proportional to the 12th power of probe-sample distance, this dependence being steeper than that found in 1-D [22] and 2-D [21] scatterers. We also note the presence of the factor $\left| \tilde{f}(\omega)\, \tilde{f}(\omega_S) \right|^2$ which, for $\tilde{f}(\omega) \cong \tilde{f}(\omega_S)$ (usually valid for Raman scattering), reduces to $\left| \tilde{f}(\omega) \right|^4$, usually identified as the overall enhancement factor in near-field Raman experiments. However, we note that if the Raman modes of interest have a rather large spectral separation, the wavelength dependence of the plasmons activated at the probe apex may start to play a non-negligible role on the different enhancement experienced by each mode. Additionally, the analytical formula shown here allows us to highlight the importance of taking into account both the probe dipole orientation and the Raman tensors in the interpretation of the experimental overall enhancement factors, which may vary significantly depending on these properties.

III. POINT DEFECTS IN GRAPHENE AND SP² CARBON MATERIALS

Motivated by the general interest in Raman characterization of defective graphene[29] and other 2-D materials[30], and in particular by our recent experimental report on the nanoscale mapping of individual point defects[9], in this section we apply the model presented in section II to point defects in graphene, which may be regarded as 0-D scatterers. We briefly recall the origin of the main Raman peaks in graphene. The G-peak is associated to Γ-point optical phonons (i.e. the center of the Brillouin zone) and it is due to in-plane vibrations of carbon pairs [31] . The D-peak is associated to transverse optical phonons at the K-point (away from Γ); therefore it is not normally activated in pristine graphene[31]. However, it can become active due to a double resonance mechanism aided by the breaking of translational symmetry of the crystal, i.e. in the vicinity of edges or defects[31]. Spatially, the D-peak is highly localized at the edges or defects within 2-3 nm from the defective structure[9]. For example, the D-peak can be spatially localized in a nanometer-sized area around a vacancy point-like defect, which *de facto* acts as a point Raman source for the typical spatial resolution of near-field spectroscopy (≈20 nm).

In Fig.2 we show the spatial Raman maps arising from the D-peak of a point defect in graphene, computed using Eq. 1, for different orientations of the incident field and of the probe. We fixed the azimuthal angles ϕ=β=0° and the electric field angle γ=30°, whilst moving the angle of the probe, θ, in the *xz* plane. The intensity is calculated by varying the position of the point defect in the *xy* plane, i.e. $\mathbf{r}'$. In the computation we used the Raman tensor for the A_{1g} symmetry associated to the D-peak:

$$\bar{\bar{\boldsymbol{\alpha}}}_{\mathrm{D}}(\omega_S, \omega) = \alpha_{\mathrm{D}} \begin{pmatrix} 1 & 0 & 0 \\ 0 & 1 & 0 \\ 0 & 0 & 0 \end{pmatrix}, \tag{3}$$

where α_{D} is a constant, and $\hat{\mathbf{x}}$, $\hat{\mathbf{y}}$ and $\hat{\mathbf{z}}$ were fixed as the principal axes of the crystal. For the curvature radius of the probe apex and for the probe-scatterer distance we used typical experimental geometry parameters, i.e. ρ=20 nm and Δ=1 nm, respectively.

As shown in Fig. 2, when the probe is perpendicular to the sample ($\theta = 0°$), the TERS intensity pattern resembles a circular ring. For a slight tilting angle, which is inevitably present in experimental conditions[32], an asymmetry starts developing in the TERS pattern which becomes a single (and slightly asymmetric) peak for the probe approaching a direction parallel to the sample. The image shape is independent on the electric field orientation (i.e. β and γ) whose only role is to affect the efficiency of the excitation of the probe dipole, and therefore the overall TERS intensity. We note also that the patterns obtained in Fig. 2 reflect the probe dipole field distribution, and in particular the intensity of the in-plane electric field component incident on the sample. This is due to the structure of the A_{1g} Raman tensor applied here, where only the diagonal components are not zero. In general, more complex shapes are expected for different Raman tensors (see Sec. IV).

In the literature it is often assumed that the resolution of a TERS image is equivalent to the extent of electric field enhancement around the probe or the probe apex radius[19]. From the patterns calculated with the model we find that the resolution is greatly affected by the probe angle, a phenomenon neglected in literature so far, yet in experimental studies the probe is seldom oriented normal to the sample surface[32]. For example, in our calculation, the spatial extent of the near-field Raman signal (which, in practice, corresponds to the mapping resolution) ranges between ~2(Δ+ρ) for $\theta = 0°$ (ring-like map) and ~(Δ+ρ)/2 for $\theta \cong 90°$ (a single maximum), as shown in the line profiles of Fig. 2. Moreover, in the case of highly tilted probes (large θ), the intensity maximum occurs when the location of the probe is shifted from that of the scatterer.

Fig. 3 shows the dependence of the maximum TERS intensity that can be obtained in a single map on the respective orientation of the probe and electric field. We first analyze the effect of the tilting angles for the electric field and the probe, by keeping the azimuthal angles fixed (ϕ=β=0°). In order to maximize the intensity, the condition $\gamma \cong \theta$ needs to be satisfied for high tilting angle of the electric field ($\gamma \to 90°$). When γ is lowered, the maximum intensity is achieved for θ increasingly higher than γ, and, in the limit $\gamma = 0°$, it is achieved for $\theta \cong 20°$. This trend arises as a consequence of the trade-off that needs to be reached between the condition of maximum enhancement of the exciting light ($\gamma = \theta$) and of the Raman scattering ($\theta = 90°$ for in-plane modes). Therefore, given a certain excitation incidence, the angle of the probe needs to be calibrated taking the polarizability of the sample into account. We note that in the available literature it is often assumed that probe axis and incident electric field need to be aligned[33] and the effect introduced by the specific Raman tensor is neglected. For the sake of completeness we also show in Fig.3b the relation between the maximum TERS intensity and the azimuthal angles of the probe and the electric field (that is, their orientation with respect to one another and to the Raman tensor principal axes), which needs to satisfy the condition ϕ=β in order for the enhancement to be maximized. We note that the graph is plotted by keeping $\theta = \gamma = 45°$ fixed; however the shape of the plot is independent of these angles

We note that knowledge of the orientation of the incident electric field at the probe axis ($\mathbf{E_i}(\mathbf{r_z}, \omega)$ in Eq.1) is required in order to compute correctly the relative Raman intensity when the probe angle is varied. However, although a focused laser beam is characterized by a dominant polarization of the electric field, a distribution of polarizations occurs on the focal plane of a highly focused Gaussian beam [23]. As a consequence, the polarization of $\mathbf{E_i}(\mathbf{r_z}, \omega)$ is dependent on the alignment of the probe apex with the focused laser beam. From the experimental point of view, the probe apex can be illuminated sideways by a linearly polarized beam (reflection mode), or through a transparent substrate by a tightly focused radially polarized beam (transmission mode). The field strength of the spurious component of $\mathbf{E_i}$ will depend on the numerical aperture NA of the objective lens and on the index of refraction *n* of the medium. To discuss the contribution of the spurious components, we can analyze the case of NA=1.4 and *n*=1.5, and a beam waist matching with the back aperture of the objective. For an *x*-polarized focused Gaussian beam, in the worst case scenario[34] (i.e. the case when the deviation from the dominant polarization is highest, occurring in specific points within the focal plane), we have $|\mathrm{E}_y|^2 \cong 0.003\,|\mathrm{E}_x|^2$ and $|\mathrm{E}_z|^2 \cong 0.12\,|\mathrm{E}_x|^2$. When a radially polarized beam is focused, the center of the focal spot is dominated by the component E_z, whereas the intensity of the transverse component $\mathrm{E}_{||}$ dominates as one moves away from the center, in a ring-like shape. In the worst case scenario, one has[34] $|\mathrm{E}_{||}|^2 \cong 0.3\,|\mathrm{E}_z|^2$. In practice, the orientation of $\mathbf{E_i}$ can be affected by misalignment more effectively when radial polarization is used in comparison to linear polarization.

IV. EFFECT OF RAMAN TENSOR ON NEAR-FIELD RAMAN MAPPING: BIOMOLECULES

In this section, the model presented in section II is extended to the study of the Raman tensor of a generic 0-D scatterer, demonstrating how the symmetry of the Raman tensor is reflected in the near-field map. For the sake of simplicity, the probe is kept fixed and oriented along the *z*-axis, whereas the Raman tensor is varied. For the scope of the discussion presented in this section, the orientation of the incident electric field is not strictly relevant, as it will influence only the near-field Raman intensity and not the spatial form of the near-field maps. We will consider a general diagonalized Raman tensor of the form

$$\bar{\bar{\boldsymbol{\alpha}}}_{\mathrm{R}}^{0}(\omega_{\mathrm{S}}, \omega) = \begin{pmatrix} \alpha_1 & 0 & 0 \\ 0 & \alpha_2 & 0 \\ 0 & 0 & \alpha_3 \end{pmatrix} \tag{4}$$

with respect to a set of principal axes *x*', *y*' and *z*', of the particular Raman active mode, such that the Raman tensor can be expressed using a transformation matrix $\bar{\bar{\mathbf{R}}}$ as:

$$\bar{\bar{\boldsymbol{\alpha}}}_{\mathrm{R}}(\omega_{\mathrm{S}}, \omega) = \bar{\bar{\mathbf{R}}}^{\mathbf{T}} \cdot \bar{\bar{\boldsymbol{\alpha}}}_{\mathrm{R}}^{0} \cdot \bar{\bar{\mathbf{R}}}\,. \tag{5}$$

For our purposes only the relative magnitude of the tensor elements are relevant, therefore we define

$$r_1 = \frac{\alpha_1}{\alpha_3} \text{ and } \; r_2 = \frac{\alpha_2}{\alpha_3}\,, \tag{6}$$

which totally describe the Raman tensors. A possible graphical visualization capturing $\bar{\bar{\boldsymbol{\alpha}}}_{\mathrm{R}}^{0}$, can be constructed by plotting the polarized Raman intensity[24]

$$I = |\mathbf{e} \cdot \bar{\bar{\boldsymbol{\alpha}}}_{\mathrm{R}}^{0} \cdot \mathbf{e}|^2 \tag{7}$$

where $\mathbf{e}$ is a unit vector rotating in the xyz space. In other terms, the spatial plot of *I* could be generated with an ideal experiment where the excitation and collection polarizers, are varied in all the directions, while kept parallel to each other.

Biomolecules are of particular interest for TERS, which could be used to distinguish individual DNA and RNA bases[35,36]. DNA bases are a valuable example for our purpose, as they have planar structures and can be deposited flat on a surface. In Fig. 4 we present calculated TERS maps of the four DNA bases (adenine, cytosine, guanine, thymine), along with another widely studied molecule, tyrosine. We have also calculated the TERS map for the peptide amide III band. The principal axes (blue and red arrows), and the corresponding values of r_1 and r_2 for specific Raman modes (indicated by the blue and red numerical values, respectively), are also shown in Fig. 4, as reported in polarization studies which can be found in literature[37].

For each Raman mode of the selected molecules, we report both the spherical plot of Eq. 7, and the spatial TERS map computed using Eq. 1. We note a qualitative resemblance between the two spatial distributions of the plots, which allows us to gain information about the structure of the Raman tensor giving rise to a specific vibration in a molecule, via inspection of the spatial TERS map experimentally acquired on the molecule.

The determination of Raman tensors of molecules is not usually straightforward. An experimental method[37,38] to determine the tensor elements requires polarized measurements on a crystalline molecular structure, as well as calculation of the depolarization ratio, as given by cross-polarized measurements on randomly oriented molecules[39]. This approach makes the determination of the principal axes of the molecule as well as its tensor elements possible, however multiple measurements on different samples may be required. On the

theoretical side, *ab initio* molecular orbital calculations can also be employed[40,41]. In contrast, here we have shown that the symmetry of the Raman tensor can be qualitatively inferred by acquiring the near-field intensity map of its related molecular vibration.

We note that the validity of our framework holds under the assumption of non-resonant Raman scattering. Ref.[42] has reported the onset of modifications in the symmetry of the Raman tensors of molecules, induced by resonance or near-resonance conditions. This was ascribed to the fact that resonance phenomena can modify the molecule depolarization ratios, hence the intrinsic symmetry of the Raman modes. The Raman tensors used in our work are those obtained in off-resonance conditions, while Raman tensors determined in conditions of resonant excitation may have a different symmetry and are not discussed here.

V. TIP-ENHANCED RAMAN SCATTERING AND FLUORESCENCE – A QUALITATIVE COMPARISON

The TERS patterns presented in Section III-IV share qualitative analogies with the near-field fluorescence images of molecules and quantum dots; however, it is important to emphasize that the physical mechanism involved in these two optical processes is intrinsically different. Fluorescence imaging has been reported in the literature using near-field techniques such as near-field scanning optical microscopy (NSOM)[43] and tip-enhanced fluorescence[44].

NSOM utilizes a sub-wavelength aperture at the end of a fiber guiding the exciting light, whose polarization determines the fluorescence intensity pattern. In tip-enhanced fluorescence microscopy, the intensity patterns are determined by the near-field generated by a sharp probe which is, to a good approximation, a dipolar field[32]. As a consequence, the intensity patterns in tip-enhanced fluorescence are less dependent on the spatial envelope of the incident field, as long as there is a sufficient z-component of polarisation in the incident field to induce a strong field enhancement. We also note that metal probes, when placed in close proximity to a molecule (at a distance of few nanometers), can decrease the molecular quantum yield, resulting in a quenching of fluorescence[45,46] and quantitatively affecting the tip-enhanced fluorescence patterns.

Moreover, while a fluorescent molecule is described well by a single dipole, which can be described by a uniaxial tensor, the case of Raman scattering is qualitatively more complex. Here we have calculated the Raman intensity patterns of molecules for a range of Raman tensor and have demonstrated that the symmetry of the Raman tensor has a significant impact on the TERS intensity pattern. The differences between the intensity patterns of molecules with different Raman tensors are distinctive, and this can potentially be used to distinguish different molecules with different types of Raman tensors, or even different Raman modes within the same molecule.

VI. CONCLUSION

In conclusion, we have studied the tip-enhanced Raman scattering patterns of zero-dimensional sources, such as localized Raman modes within a crystal, molecules, nanoparticles etc. We first applied a model based on dipole-dipole interaction to the study of the Raman D-peak originated from point defects in graphene, carbon nanotubes and sp^2 carbon materials in general. The optimal angle of the probe (maximizing the enhancement) is found to be dependent not only on the excitation incidence, as commonly accepted, but also on the Raman polarizability. The TERS patterns were also found to be sensitive to the probe orientation, thus determining the spatial resolution. The model was then applied to the study of representative biological molecules with a fixed, but arbitrary, orientation and for a range of Raman tensor symmetries. The results can be used to determine the orientation of single molecules and differentiate molecules with diverse Raman tensors, or Raman modes with different Raman tensors from the same molecule.

ASSOCIATED CONTENT

Supporting Information. Further details on the analytical model used in this work, including the derivation of eq 1.

ACKNOWLEDGMENTS

SM and DR acknowledge financial support from the Innovation Research and Development Programme of the National Measurement System, UK, Project No. 115948.

REFERENCES

(1) Zayats, A.; Richards, D. *Nano-Optics and near-Field Optical Microscopy*; Artech House, 2009.

(2) Kumar, N.; Mignuzzi, S.; Su, W.; Roy, D. Tip-Enhanced Raman Spectroscopy: Principles and Applications. *EPJ Tech. Instrum.* **2015**, *2* (1), 9.

(3) Verma, P.; Yamada, K.; Watanabe, H.; Inouye, Y.; Kawata, S. Near-Field Raman Scattering Investigation of Tip Effects on C60 Molecules. *Phys. Rev. B - Condens. Matter Mater. Phys.* **2006**, *73* (4), 45416.

(4) Zhang, R.; Zhang, Y.; Dong, Z. C.; Jiang, S.; Zhang, C.; Chen, L. G.; Zhang, L.; Liao, Y.; Aizpurua, J.; Luo, Y.; et al. Chemical Mapping of a Single Molecule by Plasmon-Enhanced Raman Scattering. *Nature* **2013**, *498* (7452), 82–86.

(5) Sonntag, M. D.; Klingsporn, J. M.; Garibay, L. K.; Roberts, J. M.; Dieringer, J. a.; Seideman, T.; Scheidt, K. a.; Jensen, L.; Schatz, G. C.; Van Duyne, R. P. Single-Molecule Tip-Enhanced Raman Spectroscopy. *J. Phys. Chem. C* **2012**, *116* (1), 478–483.

(6) Jiang, N.; Foley, E. T.; Klingsporn, J. M.; Sonntag, M. D.; Valley, N. a; Dieringer, J. a; Seideman, T.; Schatz, G. C.; Hersam, M. C.; Van Duyne, R. P. Observation of Multiple Vibrational Modes in Ultrahigh Vacuum Tip-Enhanced Raman Spectroscopy Combined with Molecular-Resolution Scanning Tunneling Microscopy. *Nano Lett.* **2012**, *12* (10), 5061–5067.

(7) Zhang, W.; Yeo, B. S. B. S.; Schmid, T.; Zenobi, R. Single Molecule Tip-Enhanced Raman Spectroscopy with Silver Tips. *J. Phys. Chem. C* **2007**, *111* (4), 1733–1738.

(8) Steidtner, J.; Pettinger, B. Tip-Enhanced Raman Spectroscopy and Microscopy on Single Dye Molecules with 15 Nm Resolution. *Phys. Rev. Lett.* **2008**, *100* (23), 236101.

(9) Mignuzzi, S.; Kumar, N.; Brennan, B.; Gilmore, I.; Richards, D.; Pollard, A. J.; Roy, D. Probing Individual Point Defects in Graphene via near-Field Raman Scattering. *Nanoscale* **2015**, *7*, 19413.

(10) Okuno, Y.; Saito, Y.; Kawata, S.; Verma, P. Tip-Enhanced Raman Investigation of Extremely Localized Semiconductor-to-Metal Transition of a Carbon Nanotube. *Phys. Rev. Lett.* **2013**, *111* (21), 216101.

(11) Pollard, A. J.; Kumar, N.; Rae, A.; Mignuzzi, S.; Su, W.; Roy, D. Nanoscale Optical Spectroscopy: An Emerging

Tool for the Characterization of Graphene and Related 2-D Materials. *J. Mater. Nanosci.* **2014**, *1* (1), 39–49.

(12) Yano, T.-A.; Ichimura, T.; Kuwahara, S.; H'dhili, F.; Uetsuki, K.; Okuno, Y.; Verma, P.; Kawata, S. Tip-Enhanced Nano-Raman Analytical Imaging of Locally Induced Strain Distribution in Carbon Nanotubes. *Nat. Commun.* **2013**, *4*, 2592.

(13) Chen, C.; Hayazawa, N.; Kawata, S. A 1.7 Nm Resolution Chemical Analysis of Carbon Nanotubes by Tip-Enhanced Raman Imaging in the Ambient. *Nat. Commun.* **2014**, *5*, 3312.

(14) Bao, W.; Borys, N. J.; Ko, C.; Suh, J.; Fan, W.; Thron, A.; Zhang, Y.; Buyanin, A.; Zhang, J.; Cabrini, S.; et al. Visualizing Nanoscale Excitonic Relaxation Properties of Disordered Edges and Grain Boundaries in Monolayer Molybdenum Disulfide. *Nat. Commun.* **2015**, *6*, 7993.

(15) Su, W.; Kumar, N.; Mignuzzi, S.; Crain, J.; Roy, D. Nanoscale Mapping of Excitonic Processes in Single Layer MoS 2 Using Tip-Enhanced Photoluminescence Microscopy. *Nanoscale* **2016**.

(16) Georgi, C.; Hartschuh, A. Tip-Enhanced Raman Spectroscopic Imaging of Localized Defects in Carbon Nanotubes. *Appl. Phys. Lett.* **2010**, *97* (14), 143117.

(17) Maciel, I. O.; Anderson, N.; Pimenta, M. A.; Hartschuh, A.; Qian, H.; Terrones, M.; Terrones, H.; Campos-Delgado, J.; Rao, A. M.; Novotny, L.; et al. Electron and Phonon Renormalization near Charged Defects in Carbon Nanotubes. *Nat. Mater.* **2008**, *7* (11), 878–883.

(18) Su, W.; Roy, D. Visualizing Graphene Edges Using Tip-Enhanced Raman Spectroscopy. *J. Vac. Sci. Technol. B Microelectron. Nanom. Struct.* **2013**, *31* (4), 41808.

(19) Behr, N.; Raschke, M. B. Optical Antenna Properties of Scanning Probe Tips: Plasmonic Light Scattering, Tip-Sample Coupling, and near-Field Enhancement. *J. Phys. Chem. C* **2008**, *112* (10), 3766–3773.

(20) Ossikovski, R.; Nguyen, Q.; Picardi, G. Simple Model for the Polarization Effects in Tip-Enhanced Raman Spectroscopy. *Phys. Rev. B* **2007**, *75* (4), 45412.

(21) Maximiano, R. V.; Beams, R.; Novotny, L.; Jorio, A.; Cançado, L. G. Mechanism of near-Field Raman Enhancement in Two-Dimensional Systems. *Phys. Rev. B* **2012**, *85* (23), 235434.

(22) Cançado, L. G.; Jorio, A.; Ismach, A.; Joselevich, E.; Hartschuh, A.; Novotny, L. Mechanism of Near-Field Raman Enhancement in One-Dimensional Systems. *Phys. Rev. Lett.* **2009**, *103* (18), 186101.

(23) Beams, R.; Cançado, L. G.; Oh, S.-H.; Jorio, A.; Novotny, L. Spatial Coherence in Near-Field Raman Scattering. *Phys. Rev. Lett.* **2014**, *113* (18), 186101.

(24) Cançado, L. G.; Beams, R.; Jorio, A.; Novotny, L. Theory of Spatial Coherence in Near-Field Raman Scattering. *Phys. Rev. X* **2014**, *4* (3), 31054.

(25) Gersten, J.; Nitzan, A. Electromagnetic Theory of Enhanced Raman Scattering by Molecules Adsorbed on Rough Surfaces. *J. Chem. Phys.* **1980**, *73* (7), 3023.

(26) Metiu, H. Surface Enhanced Spectroscopy. *Prog. Surf. Sci.* **1984**, *17* (3–4), 153–320.

(27) Moskovits, M.; Uersi, U. Surface-Enhanced Spectroscopy. *Rev. Mod. Phys.* **1985**, *57* (3).

(28) Hillenbrand, R.; Taubner, T.; Keilmann, F. Phonon-Enhanced Light-Matter Interaction at the Nanometre Scale. *Nature* **2002**, *418* (6894), 159–162.

(29) Lucchese, M. M.; Stavale, F.; Ferreira, E. H. M.; Vilani, C.; Moutinho, M. V. O.; Capaz, R. B.; Achete, C. A.; Jorio, A. Quantifying Ion-Induced Defects and Raman Relaxation Length in Graphene. *Carbon N. Y.* **2010**, *48* (5), 1592–1597.

(30) Mignuzzi, S.; Pollard, A. J.; Bonini, N.; Brennan, B.; Gilmore, I. S.; Pimenta, M. A.; Richards, D.; Roy, D. Effect of Disorder on Raman Scattering of Single-Layer MoS2. *Phys. Rev. B* **2015**, *91*, 195411.

(31) Ferrari, A. C.; Basko, D. M. Raman Spectroscopy as a Versatile Tool for Studying the Properties of Graphene. *Nat. Nanotechnol.* **2013**, *8* (4), 235–246.

(32) Mino, T.; Saito, Y.; Verma, P. Quantitative Analysis of Polarization- Controlled Tip-Enhanced Raman Imaging through the Evaluation of the Tip Dipole. *ACS Nano* **2014**, *8* (10), 10187–10195.

(33) Roy, D.; Williams, C. High Resolution Raman Imaging of Single Wall Carbon Nanotubes Using Electrochemically Etched Gold Tips and a Radially Polarized Annular Beam. *J. Vac. Sci. Technol. A Vacuum, Surfaces, Film.* **2010**, *28* (3), 472.

(34) Hecht, L. N. and B. *Principles of Nano-Optics*; Cambridge University Press: New York, 2006.

(35) Bailo, E.; Deckert, V. Tip-Enhanced Raman Spectroscopy of Single RNA Strands: Towards a Novel Direct-Sequencing Method. *Angew. Chem. Int. Ed. Engl.* **2008**, *47* (9), 1658–1661.

(36) Lipiec, E.; Sekine, R.; Bielecki, J.; Kwiatek, W. M.; Wood, B. R. Molecular Characterization of DNA Double Strand Breaks with Tip-Enhanced Raman Scattering. *Angew. Chemie - Int. Ed.* **2014**, *53* (1), 169–172.

(37) Tsuboi, M.; Benevides, J. M.; Thomas, G. J. Raman Tensors and Their Application in Structural Studies of Biological Systems. *Proc. Jpn. Acad. Ser. B. Phys. Biol. Sci.* **2009**, *85* (3), 83–97.

(38) Tsuboi, M.; Ueda, T.; Ushizawa, K.; Ezaki, Y.; Overman, S. a.; Thomas, G. J. Raman Tensors for the Tryptophan Side Chain in Proteins Determined by Polarized Raman Microspectroscopy of Oriented N-Acetyl-L-Tryptophan Crystals. *J. Mol. Struct.* **1996**, *379* (95), 43–50.

(39) Hayes, W.; Loudon, R. *Scattering of Light by Crystals*; John Wiley and Sons Inc., 1978.

(40) Torii, H.; Tasumi, M. Ab Initio Molecular Orbital Study of the Amide I Vibrational Interactions between the Peptide Groups in Di- and Tripeptides and Considerations on the Conformation of the Extended Helix. *J. Raman Spectrosc.* **1998**, *29* (1), 81–86.

(41) Torii, H.; Tasumi, M. Liquid Structure, Infrared and Isotropic/Anisotropic Raman Noncoincidence of the Amide I Band, and Low-Wavenumber Vibrational Spectra of Liquid Formamide: Molecular Dynamics and Ab Initio Molecular Orbital Studies. *J. Phys. Chem. B* **1998**, *102* (1), 315–321.

(42) Meyer, M.; Etchegoin, P. G.; Le Ru, E. C. Electronic Structure, Raman Tensors, and Resonance Phenomena in a Simple Molecular Model. *Am. J. Phys.* **2010**, *78* (3), 300.

(43) Betzig, E.; Chichester, R. J. Single Molecules Observed by near-Field Scanning Optical Microscopy. *Science (80-.).* **1993**, *262* (5138), 1422–1425.

(44) Huang, F. M.; Festy, F.; Richards, D. Tip-Enhanced Fluorescence Imaging of Quantum Dots. *Appl. Phys. Lett.* **2005**, *87* (18), 1–3.

(45) Anger, P.; Bharadwaj, P.; Novotny, L. Enhancement and Quenching of Single-Molecule Fluorescence. *Phys. Rev. Lett.* **2006**, *96* (11), 3–6.

(46) Huang, F. M.; Richards, D. Fluorescence Enhancement and Energy Transfer in Apertureless Scanning near-Field Optical Microscopy. *J. Opt. A Pure Appl. Opt.* **2006**, *8* (4), S234–S238.

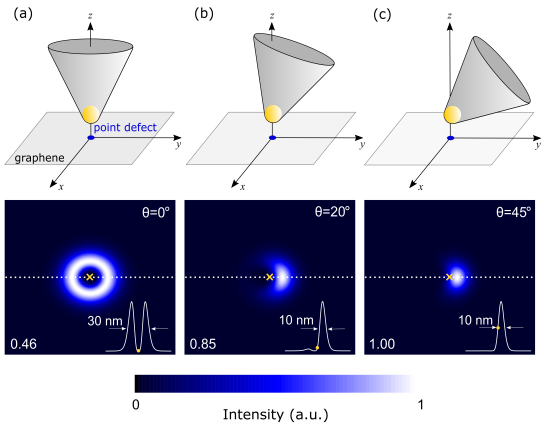

Fig. 2 Calculated near-field intensity maps of Raman D-peak from an individual point defect in graphene, for a probe of apex radius ρ =20 nm, angles of the incident electric field γ=30° and β = ϕ. The angle θ is equal to (a) 0° (b) 20° (c) 45°. In the bottom-right sections of each panel, the relative line profile corresponding to the dotted lines are indicated. Yellow symbols in the bottom panels indicate the point where the probe apex and the point defect are aligned along the *z*-axis. Relative intensities are reported in the bottom left of each figure.

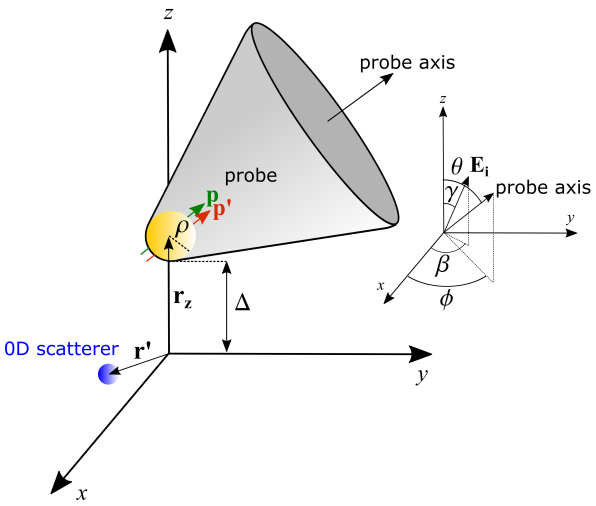

Fig. 1 Schematics of the model, representing a near-field probe on a 0-D Raman scatterer. Δ is the distance between the probe and the plane *xy*, where the 0-D Raman scatterer is located. In yellow is the probe apex, described by a curvature radius ρ. **r'** and $\mathbf{r}_z$ indicate the location of the 0-D Raman scatter and the center of the probe apex, respectively. **p** and **p'** are the dipole moments at the probe apex (see Supporting Information), aligned with the probe axis, and described by the angles θ and ϕ with respect to the *z* and *x* axes, respectively. $\mathbf{E}_i$ is the incident field described by the angles γ and β relative to the *z* and *x* axes, respectively .

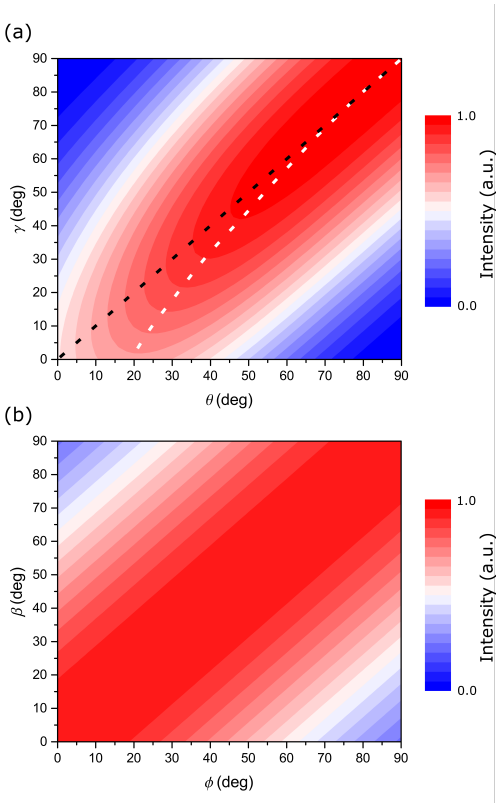

Fig. 3 Calculated maximum intensity from near-field D-peak Raman maps of an individual point defect in graphene, as a function of the (a) inclination angles and the (b) azimuthal angles of the probe and the electric field. In (a) the optimal inclination angle of the probe, given a certain inclination angle of the electric field, is marked by the white dotted line. The black dotted line indicates the condition corresponding to $\gamma = \theta$.

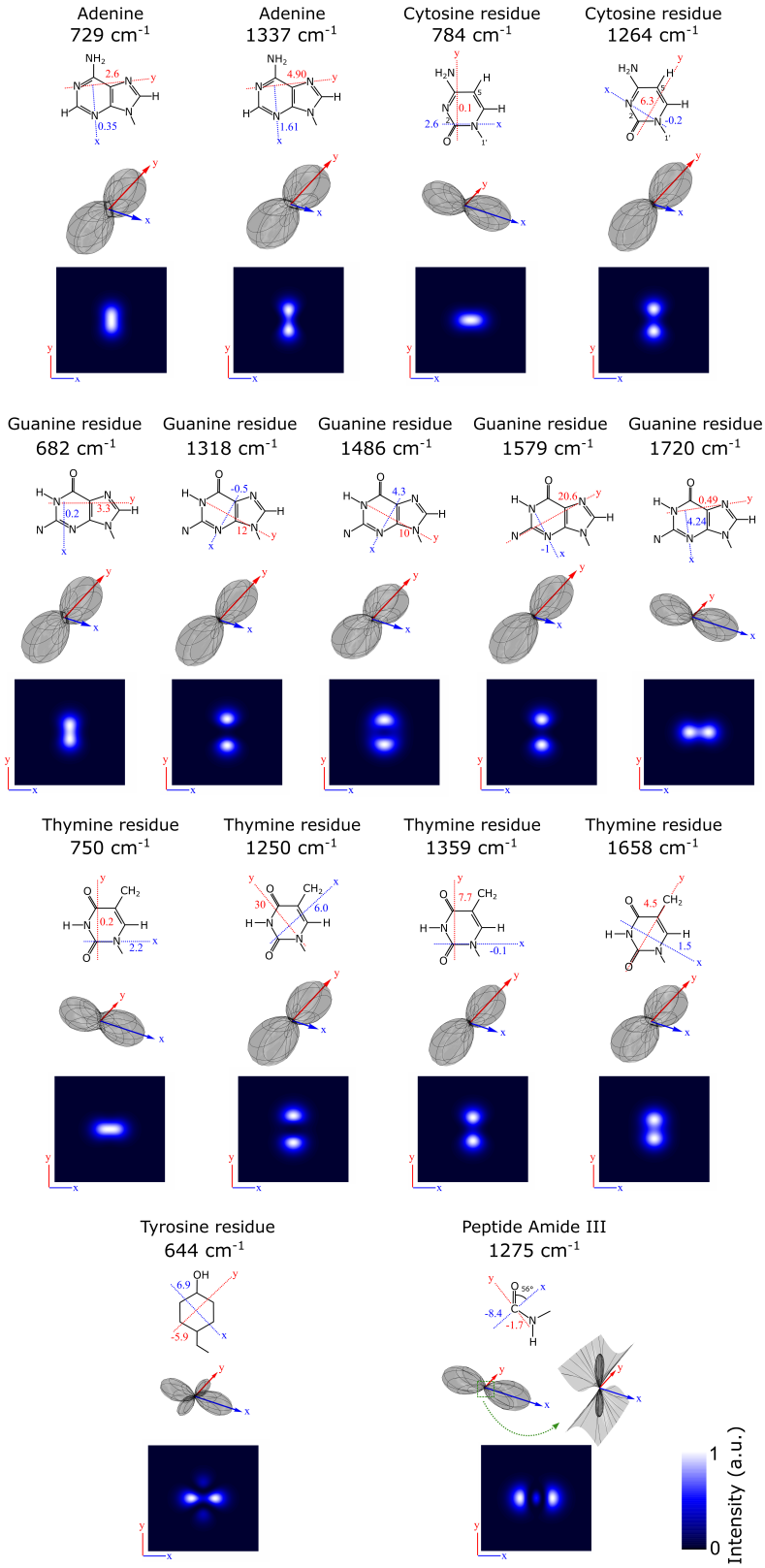

Fig. 4. Near-field Raman maps of different bands in biomolecules (Adenine, Cytosine, Guanine, Thymine, Tyrosine and peptide Amide III) and the corresponding 3D representation of the Raman tensor. Principal axes *x* and *y* and the corresponding tensor elements, as reported in Ref.[37], are indicated in blue and red respectively.